A New Single 808 nm NIR Light-Induced Imaging-Guided Multifunctional Cancer Therapy Platform

Fei He, Guixin Yang, Piaoping Yang, Yuxiu Yu, Ruichan Lv, Chunxia Li, Yunlu Dai, Shili Gai, and Jun Lin**

The NIR light-induced imaging-guided cancer therapy is a promising route in the targeting cancer therapy field. However, up to now, the existing single-modality light-induced imaging effects are not enough to meet the higher diagnosis requirement. Thus, the multifunctional cancer therapy platform with multimode light-induced imaging effects is highly desirable. In this work, captopril stabilized-Au nanoclusters $Au_{25}(Capt)_{18}$–(Au_{25}) are assembled into the mesoporous silica shell coating outside of Nd^{3+}-sensitized upconversion nanoparticles (UCNPs) for the first time. The newly formed Au_{25} shell exhibits considerable photothermal effects, bringing about the photothermal imaging and photoacoustic imaging properties, which couple with the upconversion luminescence imaging. More importantly, the three light-induced imaging effects can be simultaneously achieved by exciting with a single NIR light (808 nm), which is also the triggering factor for the photothermal and photodynamic cancer therapy. Besides, the nanoparticles can also present the magnetic resonance and computer tomography imaging effects due to the Gd^{3+} and Yb^{3+} ions in the UCNPs. Furthermore, due to the photodynamic and the photothermal effects, the nanoparticles possess efficient in vivo tumor growth inhibition under the single irradiation of 808 nm light. The multifunctional cancer therapy platform with multimode imaging effects realizes a true sense of light-induced imaging-guided cancer therapy.

1. Introduction

Multifunctional cancer therapy platforms (MCTPs) integrating imaging and therapy into a single system for imaging-guided, visualized cancer therapy have attracted significant interest in recent years due to the higher therapeutic efficiency and reduced side effects.[1–6] Phototherapy, as a class of noninvasive therapeutic techniques, has many advantages such as remote controllability, improved selectivity, and low systemic toxicity.[7–9] Compared to conventional cancer therapies including chemotherapy and radiotherapy, the phototherapy has more advantages in avoiding the toxic side effects and drug resistance.[10–12] Very recently, many works focus on introducing the phototherapy methods into some new MCTPs to pursue desirable therapeutic effects, including photothermal therapy (PTT) and photodynamic therapy (PDT).[13–17] Thereinto, to overcome the shallow tissue penetration depth and phototoxicity of the exciting light of the photosensitive drugs, some groups combined the photosensitive drugs with lanthanide ion-doped up-conversion nanoparticles (UCNPs) in the MCTPs, which are capable of emitting visible and NIR light excited with NIR radiation, and transfer the energy to the photosensitive drugs through the fluorescence resonance energy transfer (FRET).[18–21] However, due to the low quantum efficiency of the upconversion process, proper advantage is not being taken of the photosensitive drugs and the therapeutic effect is always not enough in thorough inhibition of tumor growth.[22,23] Most recently, the Nd^{3+}-sensitized UCNPs excited with 808 nm laser instead of extensively used 980 nm have drawn rather considerable interest due to its high luminescence intensity, increased penetration depth and suppressed unwanted overheating in the biological tissue.[24–27] Furthermore, the 808 nm NIR light can also be utilized as the excitation resource of some photosensitive agents, including graphene oxide, gold nanovesicles, and Au nanorods, which make it possible to achieve a dual-excitation effect to the UCNPs and photosensitive agents,[28–30] thus enhancing the therapeutic effect. On the other hand, some groups have made efforts to the combination of the PTT and PDT effects in one anticancer system for better therapeutic effect.[31–34] However, it is still highly desirable to develop a new agent with both PTT and PDT therapeutic effects and high therapeutic efficiency induced by a single excitation light.

Another advantage of the MCTPs is the multimode imaging effect, which is of special importance in the drug molecular

---

Dr. F. He, Dr. G. Yang, Prof. P. Yang, Dr. Y. Yu,
Dr. R. Lv, Dr. Y. Dai, Dr. S. Gai
Key Laboratory of Superlight Materials
and Surface Technology
Ministry of Education
College of Material Science and Chemical Engineering
Harbin Engineering University
Harbin 150001, P. R. China
E-mail: yangpiaoping@hrbeu.edu.cn
Dr. C. Li, Prof. J. Lin
State Key Laboratory of Rare Earth Resource Utilization
Changchun Institute of Applied Chemistry
Chinese Academy of Sciences
Changchun 130021, P. R. China
E-mail: jlin@ciac.ac.cn

DOI: 10.1002/adfm.201500464

© 2015 WILEY-VCH Verlag GmbH & Co. KGaA, Weinheim

tracing, cancer diagnosis, and imaging-guided therapy.[35–39] One major purpose of the multimode imaging is to integrate the advantages of each imaging technologies, such as the high temporal and spatial resolution of the computer tomography (CT) and high soft-tissue contrast and functional information in a noninvasive manner of the magnetic resonance imaging (MRI) to meet higher diagnosis requirement.[40–44] Besides, more and more efforts have been devoted to the development of the light-induced imaging technologies, such as upconversion luminescence imaging (UCL), photothermal imaging (PTI), and photoacoustic imaging (PAI) for their unique characteristics. For example, the UCL with large Stokes shift, sharp emission lines, and superior photostability properties involve the multiphoton processes of converting the low-energy photons (NIR) into high-energy photons (UV, visible, or NIR).[45–49] The PA imaging with the functions of high contrast, good spatial resolution, and deep imaging depth has proven to be a powerful technique for noninvasive visualization of tissue structures.[50–52] Finally, the PTI with real-time performance, high sensitivity properties was widely used in the imaging-guided cancer therapy, couples with the PTT.[53–55] However, due to the low spatial resolution, it is still needed to combine other light-induced imaging effects with the PTI, to achieve the imaging-guided and visualized cancer therapy.[56,57] Furthermore, the light-induced bioimaging effects can also combine with the phototherapy effects under same light radiation to achieve real-time imaging-guided cancer therapy.

In this work, we assembled captopril-stabilized Au nanoclusters (Au_{25}), a new PDT agent, onto mesoporous silica-coated Nd^{3+}-sensitized UCNPs (UCNPs@MS) to form a new multifunctional platform. The Au_{25} nanoparticles dispersed on the mesoporous silica also exhibit considerable PTT effect, which can combine with its intrinsic PDT effect to further enhance the tumor inhibition efficacies under the excitation of 808 nm laser. Furthermore, these effects can be strengthened by higher energy photons from the upconversion mechanism of the UCNPs through the FRET process. In addition, arising from the photothermal effect of the Au_{25}, the MCTPS has both PTI and PAI effects, which couple with the UCL imaging effect from the UCNPs to achieve a multimode NIR-induced imaging function.

2. Results and Discussion

2.1. Synthesis and Characterization of the Sample

The synthetic process of UCNPs@MS-Au_{25}-polyethylene glycol (PEG) is illustrated in **Figure 1**a. First, to obtain the multiple core–shell structured UCNPs, a thermal decomposition method has been adopted to prepare β-$NaGdF_4$:Yb/Er NPs. Then, two external shells including β-$NaGdF_4$:Yb and β-$NaNdF_4$:Yb from inside to outside were coated on the surface through a sequential seed-mediated process. As shown in Figure 1b,c, the average particle size of the NPs changes from 28 to 46 nm after the coating process, indicating the further crystal growth of the NPs (Figure S1, Supporting Information). Moreover, an obvious core–shell structure can be observed from the magnified transmission electron microscopy (TEM) image (inset, Figure 1c), arising from the electron penetrability of the β-$NaGdF_4$ and β-$NaNdF_4$ crystals. The coating process can further be confirmed by the X-ray powder diffraction (XRD) result. In Figure 1d, the two different patterns are consistent with the hexagonal-phased β-$NaGdF_4$ and β-$NaNdF_4$, respectively. Then the hydrophobic UCNPs dissolved in cyclohexane were transferred into hydrophilic phase using cetyltrimethyl ammonium bromide (CTAB) as the capping molecules, which also acts as the surfactant for the subsequent sol–gel reaction to form mesoporous silica shell. The removal of CTAB surfactant results in the formation of mesoporous silica shell coated on the as-obtained UCNPs (Figure 1e), which is denoted as UCNPs@MS. The as-synthesized composite possesses considerable large surface area ($582\ m^2\ g^{-1}$) and mesoporous pore structure (5.06 nm in mean pore size calculated by the Barret–Joner–Halenda (BJH) method, Figure S2, Supporting Information), which was used for loading Au_{25} agent. The as-prepared Au_{25} NPs are monodispersed with average size of 2.78 nm (Figure S3, Supporting Information), which are too small to be detected in the TEM image (Figure 1e). Before loading the Au_{25} NPs, we first treated the UCNPs@MS with poly(allylamine) (PAAm) to obtain the amino-functionalized UCNPs@MS, which can absorb the electronegative Au_{25} nanoparticles. Figure S4 (Supporting Information) gives the relative Au content of each situation after the centrifugation and redispersed processes determined by the ICP-MS, which means that the amino-functionalized UCNPs@MS is more stable for loading Au_{25} NPs. Finally, to enhance the biocompatibility of MCTPs, PEG was chosen for modifying the UCNPs@MS-Au_{25} NPs. The actual Au content is calculated to be 210 $\mu g\ mg^{-1}$ for Au/UCNPs@MS-Au_{25}-PEG determined by inductively coupled plasma mass spectrometry (ICP-MS). The energy dispersive spectrometer (EDS) element mapping can clearly show the uniform distribution of the elements in a single nanoparticle, as shown in Figure 1f. The multiple core–shell structure of UCNPs and the well-dispersed Au_{25} NPS can also be confirmed.

2.2. Singlet Oxygen Detection and Energy Transduction

The singlet oxygen ($^1O_2$) production of thiol-protected Au nanoclusters has been well demonstrated by the previous works.[58,59] On the other hand, the multiple core–shell structure of UCNPs can prevent the deleterious cross-relaxation pathways between the activator (Er^{3+}) and sensitizer (Nd^{3+}) when excited by the 808 nm laser. As shown in Figure S5 (Supporting Information), the cross-relaxation process can be markedly weakened in the multiple core–shell structured UCNPs and the UCL emission is dramatically enhanced. Therefore, the UCNPs can be excited by 980 and 808 nm laser simultaneously. When loading the captopril-protected Au_{25} into UCNPs@MS, there are two ways to achieve the FRET between UCNPs and the attached Au_{25} NPs. Hence, the PDT effect of the sample under 980 and 808 nm laser was investigated first. It is known that $^1O_2$ can react directly with 3,3′-diaminobenzidine (DAB) to form a polymer as the oxidation product and the reaction can be monitored by the changes of the absorption spectra in the UV–vis region.[60,61] So DAB was employed to examine the ability of Au_{25} to generate $^1O_2$ in aqueous media. It was found that when loading Au_{25}

© 2015 WILEY-VCH Verlag GmbH & Co. KGaA, Weinheim

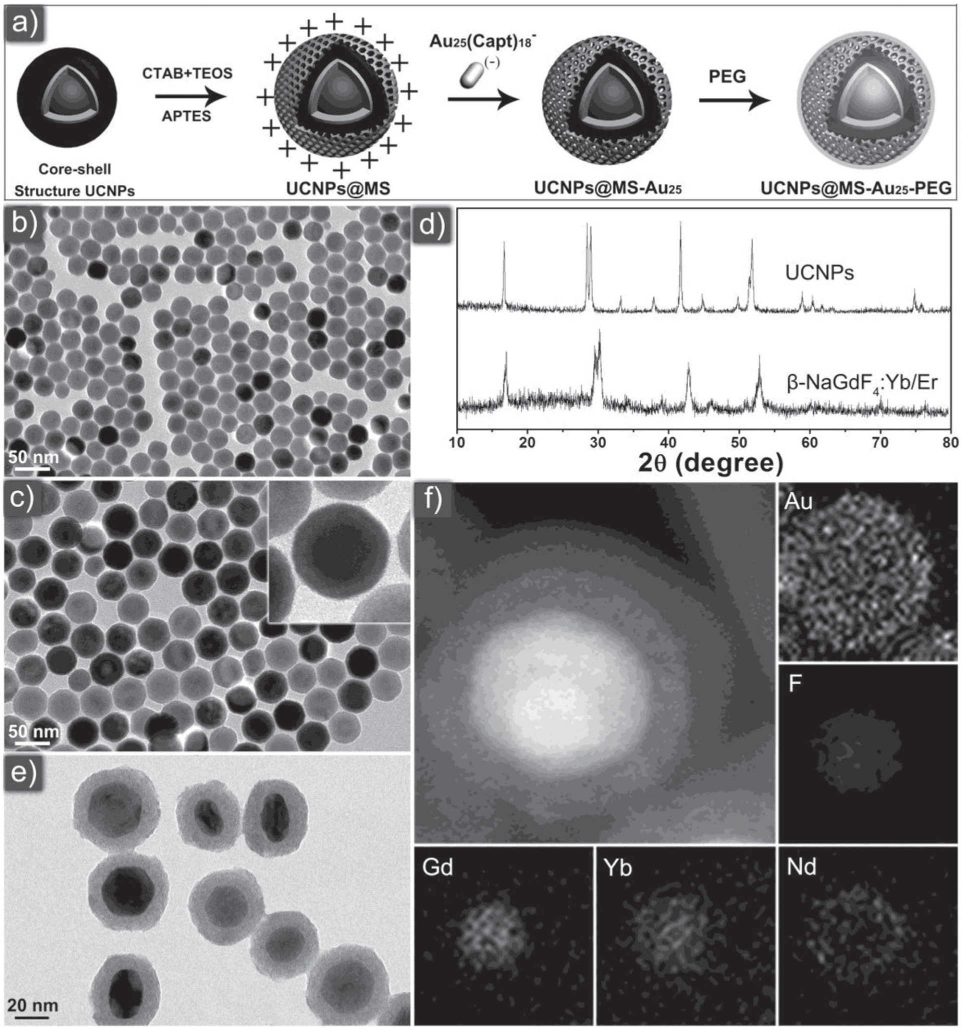

Figure 1. a) Schematic illustration for the formation of UCNPs@MS-Au_{25}-PEG. TEM images of b) β-$NaGdF_4$:Yb/Er, and c) β-$NaGdF_4$:Yb/Er@β-$NaGdF_4$:Yb@ β-$NaNdF_4$:Yb. d) XRD patterns of β-$NaGdF_4$:Yb/Er and β-$NaGdF_4$:Yb/Er@β-$NaGdF_4$:Yb@β-$NaNdF_4$:Yb. e) TEM image of UCNPs@MS. f) EDS elemental mapping of UCNPs@MS-Au_{25}-PEG. Inset in panel (c) is the magnified TEM image.

NPs, the UCL emission intensities of the sample under 980 and 808 nm are obviously decreased (**Figure 2**a,c) due to the FRET effect between the UCNPs and Au_{25} NPs. However, the sample still shows bright green emissions irradiated by both 808 and 980 nm laser (insets in Figure 2a,c). When excited by 808 nm laser, the UV–vis absorbance intensity of UCNPs@MS-Au_{25}-PEG below the wavelength of 900 nm increases markedly with the irradiation time because of the DAB oxidation (Figure 2b). The result indicates that UCNPs@MS-Au_{25}-PEG excited at 808 nm laser can effectively generate $^1O_2$, which in turn oxidize DAB, leading to increased optical absorption. The nanoparticles after the irradiation of 808 nm laser for 20 min can still keep monodispersity (Figure S6, Supporting Information), ruling out the possible influence of the aggregation of the nanoparticles to the UV–vis spectra and further confirming that the enhancement of UV–vis absorbance intensity can be ascribed to the generation of the $^1O_2$. However, when excited by 980 nm laser, the absorbance is not so high as that under the excitation of 808 nm with same irradiation time (Figure 2d), indicating a relatively low $^1O_2$ productivity. This is because that the high density 808 nm laser can be absorbed directly by the Au_{25} NPs to generate $^1O_2$, which can enhance the PDT effect to a very large extent. To study the FRET effect of UCNPs@MS-Au_{25}-PEG under excitation of 808 nm laser, we measured the emission decay curves of $^4S_{3/2} \rightarrow {}^4I_{15/2}$ (540 nm) transition in UCNPs@MS and UCNPs@MS-Au_{25}, as shown in Figure 2e, which can fit with the single exponential ($I(t) = I_0 + A_1\exp(-t/\tau_1)$) and multi-exponential ($I(t) = I_0 + A_1\exp(-t/\tau_1) + A_2\exp(-t/\tau_2)$), respectively. It is apparent that the lifetime of the $^4S_{3/2}$ state in UCNPs@MS-Au_{25} is shorter than that in UCNPs@MS. Due to the FRET effect between UCNPs and Au_{25} NPs, the energy on $^4S_{3/2}$ state can be absorbed by Au_{25} NPs and consequently reduce the lifetime (0.893 to 0.622 ms), which indicates an efficient FRET effect in UCNPs@MS-Au_{25}. The enhancing effect of the FRET to the PDT effect for the Au_{25} NPs can also be clearly confirmed by the UV–vis spectra (Figure 2f). The initial reaction rate (Q) of DAB with $^1O_2$ in the presence of $Au_{25}(Capt)_{18}$– or UCNPs@MS-Au_{25} was calculated according to the following equation[62]

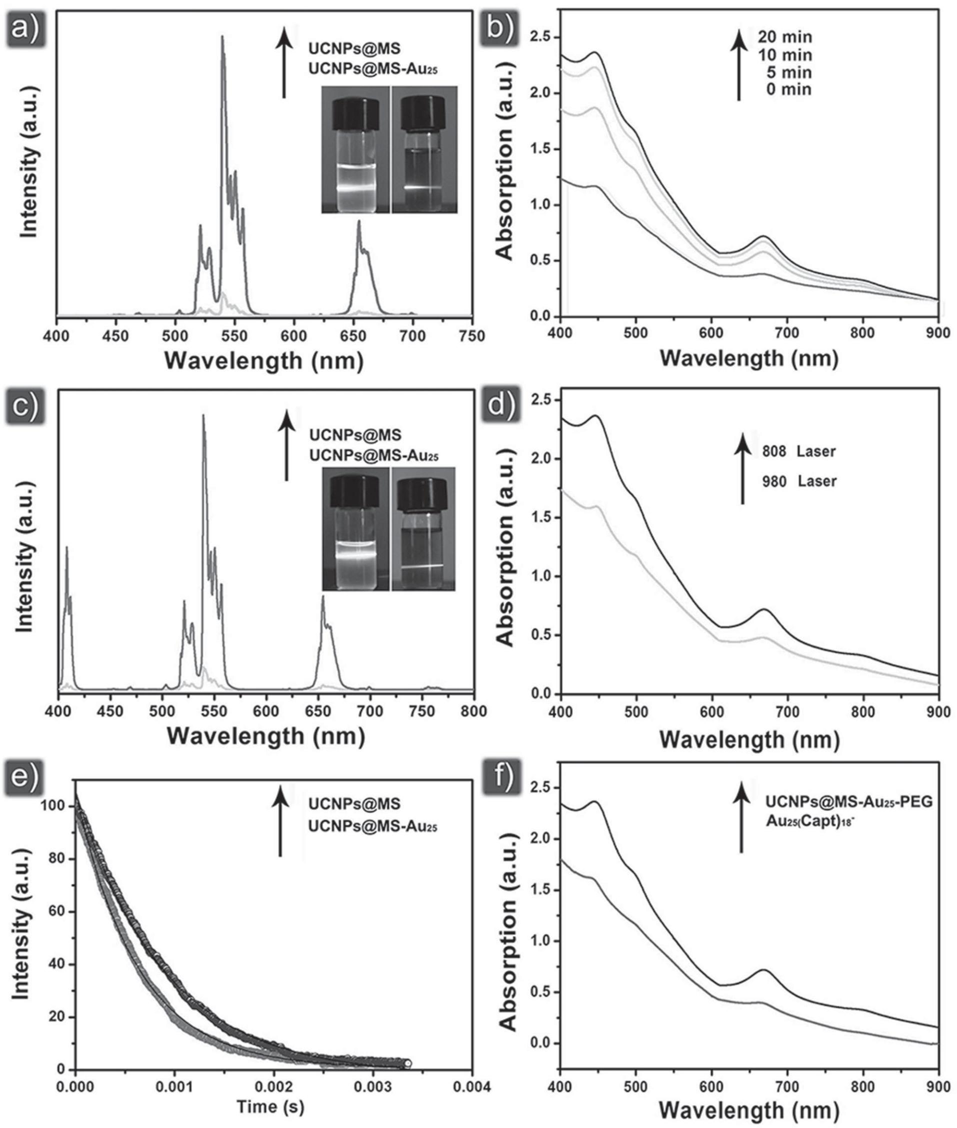

Figure 2. a) UCL emission spectra of UCNPs@MS and UCNPs@MS-Au_{25} excited by 808 nm laser, inset is the corresponding photograph under 808 nm irradiation. b) Absorption spectra of UCNPs@MS-Au_{25}-PEG in a DAB-containing solution at different irradiation time under 808 nm laser (0.5 W cm^{-2}). c) UCL emission spectra of UCNPs@MS and UCNPs@MS-Au_{25} excited by 980 nm laser, inset is the corresponding photograph under 980 nm irradiation. d) Absorption spectra of a DAB-containing solution of UCNPs@MS-Au_{25}-PEG under 808 nm laser (0.5 W cm^{-2}) and 980 nm laser (0.5 W cm^{-2}). e) Decay curves for the $^4S_{3/2} \rightarrow {}^4I_{15/2}$ emissions (540 nm) of Er^{3+} in UCNPs@MS and UCNPs@MS-Au_{25}. f) Absorption spectra of DAB-containing solutions of UCNPs@MS-Au_{25}-PEG and $Au_{25}(Capt)_{18}{}^{-}$ under 808 nm laser (0.5 W cm^{-2}) with irradiation time of 20 min and the same absorption cross-sections.

$$Q(\mathrm{UCNPs@MS{-}Au_{25}}) = R(\mathrm{UCNPs@MS{-}Au_{25}})/A(\mathrm{UCNPs@MS{-}Au_{25}}) \quad (1)$$

$Q(\mathrm{Au25}) = R(\mathrm{Au_{25}})/A(\mathrm{Au_{25}})$, in which R is the initial reaction rate of DAB with $^1O_2$ in the presence of a photosensitizer (Au_{25} or UCNPs@MS-Au_{25}). The R values were assumed to be equal to the initial slope (ΔAbs/Δtime), as shown in Figure S7 (Supporting Information). A is the absorbance at 680 nm by the photosensitizer (Au_{25} or UCNPs@MS-Au_{25}). The value of $Q(\mathrm{Au_{25}})/Q(\mathrm{UCNPs@MS\text{-}Au_{25}})$ was estimated to be 0.84, suggesting a clear improvement of the composite to the $^1O_2$ production rate. Through above analysis, it can be inferred that there are two excitation effects under the 808 nm laser irradiation, which can work together in producing $^1O_2$ and thus improve the producing efficiency.

2.3. In Vitro Toxicity and Imaging

The strong NIR absorption of UCNPs@MS-Au_{25}-PEG at 808 nm and efficient FRET between UCNPs and Au_{25} motivate us to investigate the potential in the PTT of cancer with an 808 nm laser. Moreover, the high heat stability of the Au_{25} NPs synthesized by the present method can also ensure the

© 2015 WILEY-VCH Verlag GmbH & Co. KGaA, Weinheim

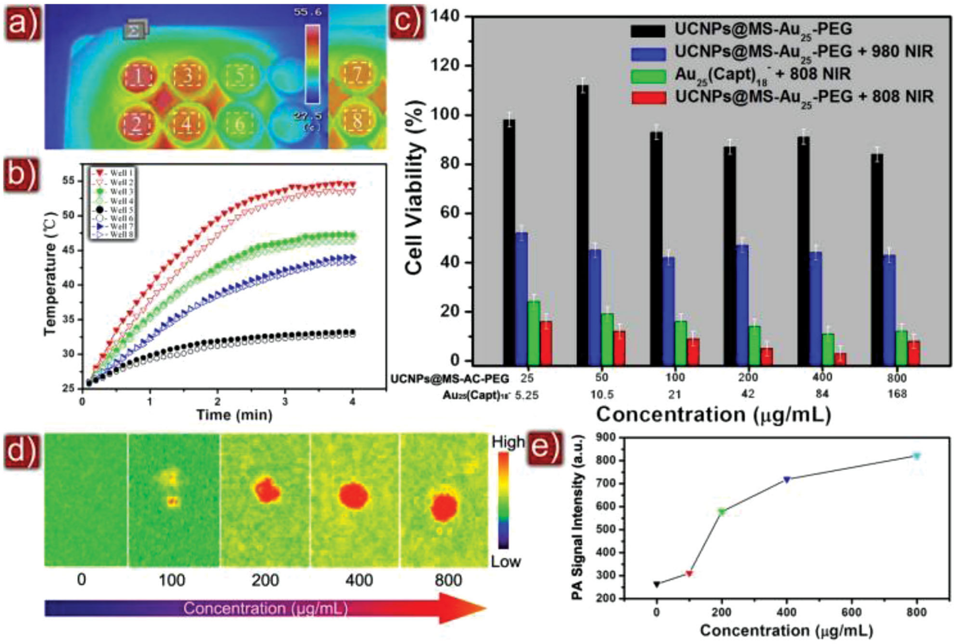

Figure 3. a) Infrared thermal photographs of a 96-well cell-culture plate of UCNPs@MS-Au$_{25}$-PEG (800 μg mL^{-1}, the well of 1, 2, 7, and 8), Au$_{25}$(Capt)$_{18}^-$ (168 μg mL^{-1}, the well of 3 and 4), culture medium (1 mL, the well of 5, 6). Note that all the samples are dissolved in culture medium containing HeLa cells. The wells of 1–6 are under 808 nm laser (2.5 W cm^{-2}) and the well of 7, 8 are under 980 nm laser (2.5 W cm^{-2}). b) Temperature profiles of the culture wells of 1–8 as a function of the laser irradiated time. c) Cell viability versus particle concentration for HeLa cells incubated under different conditions. d) PA section images of UCNPs@MS-Au$_{25}$-PEG with different concentration in distilled water. e) The corresponding PA signal intensity of UCNPs@MS-Au$_{25}$-PEG drops with different concentrations.

PDT effect in relative higher temperature.[63] We employed a series of experiments to explore the photothermal effect in vitro using HeLa cells incubated with UCNPs@MS-Au$_{25}$-PEG NPs. As shown in **Figure 3**a, 1 mL of culture medium control each was added into wells 5 and 6, while the culture medium containing UCNPs@MS-Au$_{25}$-PEG (800 μg mL^{-1}) was added into the wells 1, 2, 7, and 8, respectively. For comparison, the culture medium dispersion containing 168 μg mL^{-1} Au$_{25}$ (same Au content with UCNPs@MS-Au$_{25}$-PEG) was added into the wells 3 and 4. Two kinds of laser irradiation were executed: 808 nm laser (2.5 W cm^{-2}) to well 1–6 and 980 nm laser (2.5 W cm^{-2}) to wells 7 and 8. As expected, the UCNPs@MS-Au$_{25}$-PEG exhibits the best contrast for infrared thermal imaging (Figure 3b) due to the dual function of direct absorption of 808 nm laser and FRET effect from the UCNPs to Au$_{25}$ NPs. Under 808 nm, laser irradiation for 4 min, the mean improved temperature of wells 1 and 2 is 27.8 °C (Figure 3b), which is obviously higher than those of other wells. Before taking the particles in the cancer cell killing experiments, the in vitro cytotoxicity test was taken via the methyl thiazolyl tetrazolium (MTT) assay in L929 cells derived from human cervical carcinoma cell line. As shown in Figure S8 (Supporting Information), the cellular viability is higher than 96% after 12 h incubation with UCNPs@MS-Au$_{25}$-PEG with concentration of 0–800 μg mL^{-1}, indicating a low cytotoxicity within this concentration range. Besides, cellular uptake process of as-prepared nanoparticles was examined by using confocal laser scanning microscope (CLSM), which is shown in Figure S9 (Supporting Information). It is clear that more and more upconversion fluorescence can be detected along with the incubating time, which can further be confirmed by the experiments of the mass of gold internalized in HeLa cells (Figure S10, Supporting Information). On account of its better PDT and PTT effects when excited by 808 nm laser, the UCNPs@MS-Au$_{25}$-PEG has the best cancer killing effect than the other treatments, as shown in Figure 3c. Combined with the propidium iodide (PI) and Calcein-AM assay (Figure S11, Supporting Information), it is obvious that the HeLa cells are almost completely died when treated with UCNPs@MS-Au$_{25}$-PEG under 808 nm laser irradiation, while no obvious cell death is observed for the cells treated with UCNPs@MS-Au$_{25}$-PEG without NIR irradiation, suggesting that the cell killing effect can be ascribed to the simultaneous PDT and PTT effects. The death cells are all out of shape and obviously larger than the live cell, indicating that the cell death type is necrosis. To extend the imaging application of UCNPs@MS-Au$_{25}$-PEG, we studied the photoacoustic imaging effect in a phosphoric acidic buffer solution (PBS) solution. Interestingly, UCNPs@MS-Au$_{25}$-PEG exhibits obvious photoacoustic effect in a concentration gradient experiment under the 808 nm laser irradiation (Figure 3d,e). The single NIR light-induced tri-mode imaging effects make it possible to be used for in vivo bioimaging and imaging-guided cancer therapy.

2.4. Multimode In Vivo Imaging Effects

As an emerging bioprobe, the rare earth fluoride can act in both MRI and CT in vivo imaging probe. In the present work, the as-synthesized UCNPs@MS-Au$_{25}$-PEG also shows the MRI and CT imaging abilities (Figures S12 and S13, Supporting

© 2015 WILEY-VCH Verlag GmbH & Co. KGaA, Weinheim

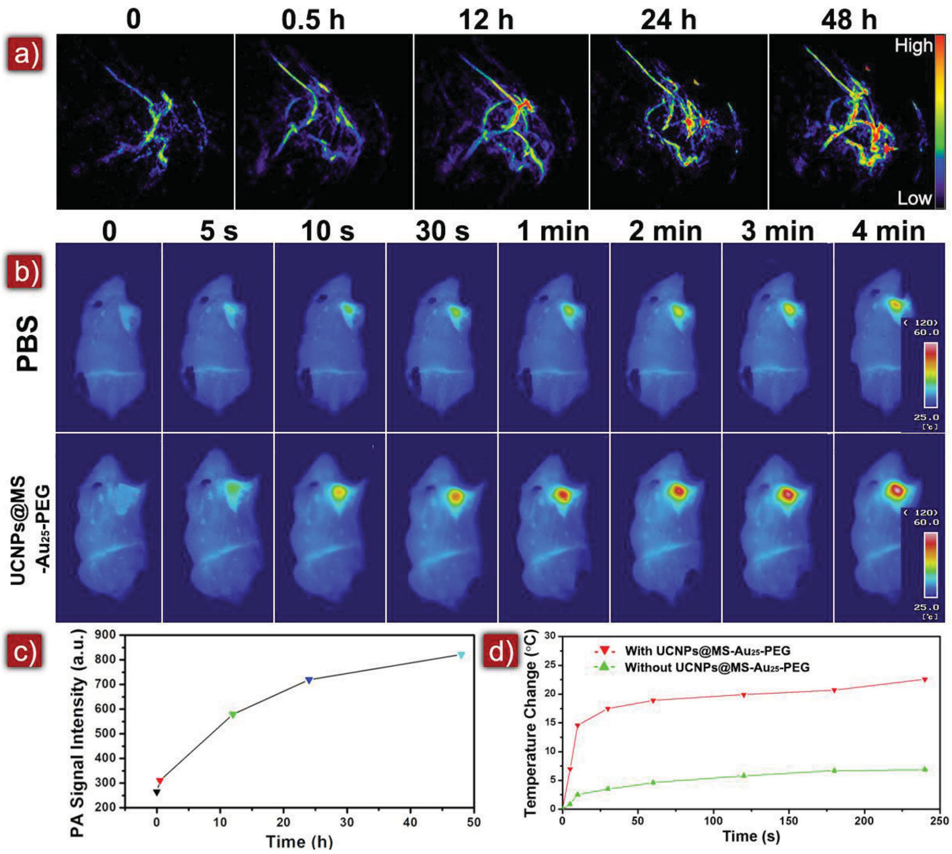

Figure 4. a) In vivo photoacoustic (PA) images of tumor tissues after the intravenous injection of UCNPs@MS-Au$_{25}$-PEG with different injection time. b) Thermal images of H22 tumor-bearing mice exposed to an 808 nm laser for 4 min after intravenous injection of phosphate-buffered saline (PBS) and UCNPs@MS-Au$_{25}$-PEG after 48 h. c) PA signal intensity of the tumors as a function of the injection time. d) Heat curves of tumors upon laser irradiation of 808 nm laser as a function of the irradiation time.

Information). For the CT imaging effect in the intravenous injection condition, it can be seen that the hounsfield unit (HU) intensities of the liver and kidney are all improved after injection of the nanoparticles (Figure S14, Supporting Information). Besides, the obvious CT contrast in the bladder can also be detected, which may be caused by the entrance of the renegade Au$_{25}$ from the nanoparticles to the bladder through the renal clearance process.[64] The transmission of the nanoparticles can be further confirmed by the PA imaging. As mentioned above, PA imaging is a promising diagnostic imaging technique due to its high resolution and noninvasive visualization of tissue structures. As shown in **Figure 4**a,c, it can be clearly observed that the PA intensity in the biotissue of tumor site is gradually improved along with the injection time, exhibiting an outstanding PA imaging effect. It is worth noting that the detailed information of the biotissue can be provided from the PA imaging, which is conducive to the cancer diagnosing and therapy. Besides, the enhanced PA signal after 48 h also indicates the continuous delivery of the nanoparticles in the mouse body. Moreover, the nanoparticles delivery status in the blood vessel and tumor tissue can also be obtained, which is of great significance in cancer therapy. The excellent PAI properties of the nanoparticles can be vividly proved by the video results (Supporting Information). Based on the PA imaging results, it is confirmable that considerable nanoparticles are gathered in the tumor site. So we conducted the in vivo PTT experiments from 48 h after intravenous injection of the nanoparticles, as shown in Figure 4b,d. It is obvious that the nanoparticles have more sensitive PTT imaging effect under the irradiation of 808 nm laser compared with the PBS. The PTT effect can be applied in both bioimaging and cancer therapy and is highly promising to achieve the light-induced therapy. However, it is worth noting that the exorbitant temperature can also harm some organ tissue, which may prevent the further application of the photothermal therapy in some cases. Besides, derived from the upconversion luminescence property, the nanoparticle can serve as the UCL probe, as shown in Figure S15 (Supporting Information), obvious green luminescence can be observed under 808 nm irradiation, which can be utilized for the tumor localization.

2.5. In Vivo Tumor Inhibition Effect

Before investigating the in vivo tumor inhibition ability of UCNPs@MS-Au$_{25}$-PEG, we first examined the blood compatibility of the sample. As shown in Figure S16 (Supporting Information), no or negligible hemolysis of red blood cells can be detected when exposed to UCNPs@MS-Au$_{25}$-PEG with concentrations ranging from 15.625 to 250 μg mL^{-1}, demonstrating an excellent blood compatibility. Further experiments were conducted to evaluate the in vivo tumor inhibition efficacy of UCNPs@MS-Au_{25}-PEG under the 808 nm laser irradiation. The liver tumor cell line H22 (murine hepatocarcinoma) was selected as the xenograft model, and the tumor-bearing Balb/c mice were divided into five groups randomly. We intravenously injected the UCNPs@MS-Au_{25}-PEG nanoparticles in the first two groups. After 48 h, the tumor site was irradiated with 808 nm laser for 30 min (2.5 W cm^{-2}, 5 min break after 10 min irradiation, group 1) and 980 nm laser for 20 min (2.5 W cm^{-2}, 5 min break after 10 min irradiation, group 2). Group 3 was injected with Au_{25} nanoparticles in the dark and irradiated with the 808 nm laser for 30 min (2.5 W cm^{-2}, 10 min break after 5 min irradiation). The injected Au dose in 80 µL of saline is 0.65 mg kg^{-1} body weight. Similar to group 1, group 4 was exposed to the 808 nm laser for 30 min without injection. Group 5 was only intravenously injected with saline (80 µL) as the control. In **Figure 5**a–c, the group treated with UCNPs@MS-Au_{25}-PEG under 808 nm laser irradiation exhibits the best tumor growth inhibition efficacy. The digital photographs of representative mice with excised tumors (Figure 5b) also show that the tumor size injected with UCNPs@MS-Au_{25}-PEG under 808 nm laser irradiation treatments is much smaller than those of other groups. The pure 808 nm laser irradiation (group 4) has no obvious effect on the tumor size. In addition, the body weight is an important parameter to evaluate the systemic toxicity of the material to the body. As given in Figure 5c, the body weight of all groups does not decrease with the prolonged time, indicating the little adverse side effect of UCNPs@MS-Au_{25}-PEG compared with traditional chemical anticancer drugs. The destructive effect of the laser to the skin at the tumor site of the mouse was also studied. In Figure 5d, the skin after irradiation treatment of the 808 nm laser keeps the original appearance while the skin treated by the 980 nm laser turns black, indicating a damaged effect. This is because the 808 nm light has less damage effect to the skin than the 980 nm laser.[24] Therefore, we have to reduce the irradiation time of the density of 980 nm laser and improve the break time simultaneously to guarantee the curative effect during the treatment process. We took the histological analysis on tumor, heart, liver, spleen, lung, and kidney in different treatment groups after 14 d of the post-treatment. It is obvious that markedly increased apoptotic and necrotic tumor cells can be observed in the first three treatment groups (Figure 5e), which can be due to the PDT and PTT effects in the phototherapy treatments. Histological analysis in Figure S17 (Supporting Information) reveals no

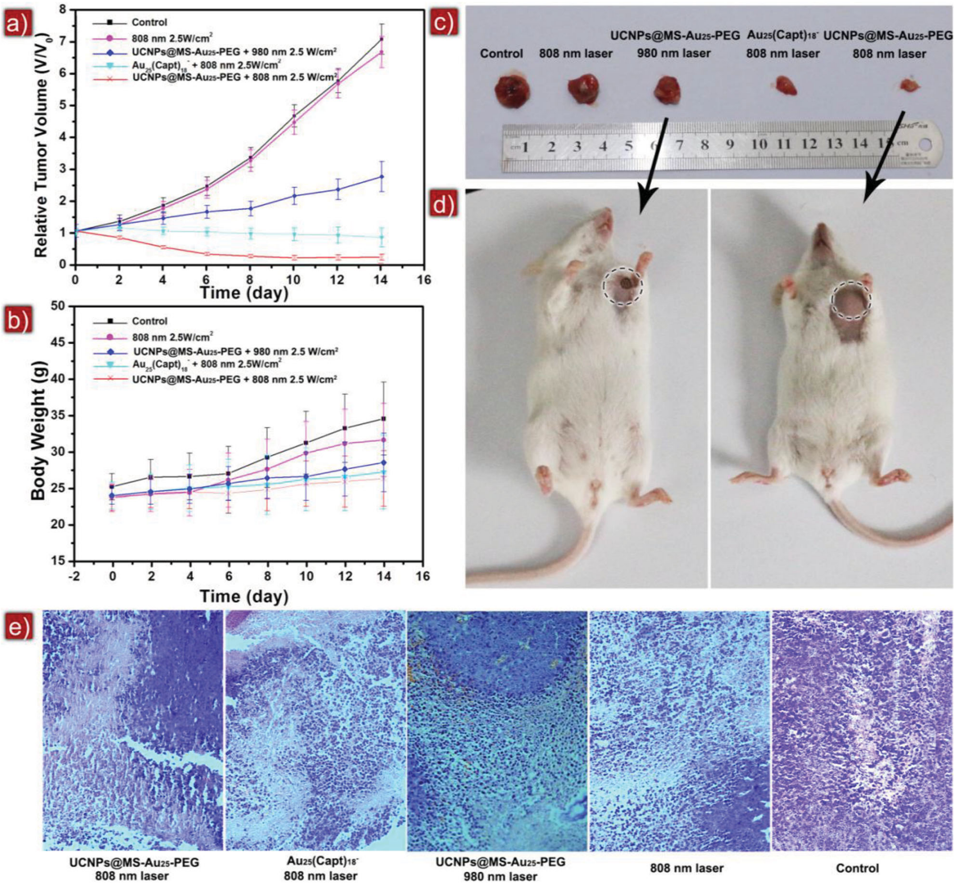

Figure 5. a) In vivo tumor volume changes of Balb/c mice on different groups after various treatments. b) The relative tumor volumes were normalized to their initial volumes before the treatment. Body weight changes with time of Balb/c mice under different treatments. Error bars indicate standard deviations. c) Photographs of excised tumors from representative Balb/c mice after 14 d treatment and d) the corresponding images of digital photos of mice after treatments. e) H&E-stained tumor sections after 14 d treatment from different groups.

© 2015 WILEY-VCH Verlag GmbH & Co. KGaA, Weinheim

pathological changes can be found in the heart, lung, kidney, liver, and spleen. In addition, ICP-MS was applied to determine in vivo long-term tissue biodistribution of UCNPs@MS-Au_{25}-PEG nanoparticles in mice, as given in Figure S18 (Supporting Information). In the early stages after the injection, the nanoparticles are accumulated in the lungs. High concentrations of Gd are detected in liver, spleen, and lung after injection of the nanoparticles for 1 h. Meanwhile, the concentrations of nanoparticles are very low in heart and kidney at all time points after postinjection. Nanoparticles accumulate in the spleen within 24 h postinjection, which may be due to that the spleen is the largest organ of the immune system. After 24 h postinjection, the concentrations of nanoparticles decrease in liver, spleen, and lung. After 7 d, the nanoparticles in the liver, spleen, and lung are much less than the first 24 h. From the change of nanoparticles in the organs, it is seen that the nanoparticles could generally be excreted from the mice as time prolonged. The results above clearly indicate the potential clinical applicability of UCNPs@MS-Au_{25}-PEG as cancer therapy agents.

3. Conclusion

In summary, the Au nanoclusters nanoparticles with PDT and PTT effects were combined with UCNPs for the first time to form a new multifunctional cancer therapy platform with multimode imaging and dual phototherapy function. The UCL process in this platform was utilized as a taken advantage of strengthen of the PDT and PTT effects by FRET effect. Except for the CT and MRI imaging effects, the UCNPs@MS-Au_{25}-PEG can also exhibit UCL, PTT, and PA imaging effects in vivo. More importantly, these three light-induced imaging effects can be simultaneously achieved by exciting with a single light (808 nm), which is also the triggering factor for the PTT and PDT cancer therapy. A series of in vivo experiments confirm the multimode imaging functions and the tumor inhibition ability of the UCNPs@MS-Au_{25}-PEG. Therefore, we believe that this new multifunctional cancer therapy platform could be a promising one to achieve the light-induced and imaging-guided cancer therapy with low side effects.

4. Experimental Section

Reagents and Materials: Y_2O_3 (99.99%), Gd_2O_3 (99.99%), Yb_2O_3 (99.99%), and Tm_2O_3 (99.99%) were purchased from Sinopharm Chemical Reagent Co., Ltd. Oleic acid (OA), 1-octadecene (ODE), tetraoctylammonium bromide (TOAB), DAB, PAAm, captopril, and PEG were purchased from Sigma-Aldrich. Dimethyl sulfoxide (DMSO), methanol, $HAuCl_4{\cdot}3H_2O$, hydroxide (H_2O_2) (30% in H_2O), and HNO_3 were purchased from Beijing Chemical Regent Co., Ltd. PEG500–silane was obtained from Beijing Kaizheng Biotech Development Co., Ltd. All the above chemicals were used as received without further purification.

Synthesis of Oleic-Acid-Stabilized β-NaGdF$_4$:Yb/Er: In a typical procedure of preparing β-$NaGdF_4$:Yb/Er, 1 mmol of RE(oleate)$_3$ (RE = 79% Gd + 20% Yb + 1% Er), 12 mmol of NaF, and 20 mL of oleic acid (OA)/1-octadecene (ODE) (v/v = 1:1) mixed solvent were added to the reaction vessel and heated to 110 °C under a vacuum for 30 min to remove residual water and oxygen. After that, the temperature was increased to 310 °C and kept for 1.5 h in N_2 atmosphere environment. The β-$NaGdF_4$:Yb^{3+}/Er^{3+} nanoparticles were obtained.

Synthesis of Oleic-Acid-Stabilized Core–Shell Structured β-NaGdF$_4$:Yb/Er@β-NaGdF$_4$:Yb@β-NaNdF$_4$:Yb Nanoparticles (UCNPs): First, the above-mentioned experiment was carried out. The cyclohexane solution of above was added to a four-neck reaction vessel. 10 mL of OA and 10 mL of ODE were added to the vessel, and the solvent was heated to 120 °C under a vacuum with magnetic stirring for 1 h and flushed with N_2. Then, the temperature was heated to 310 °C. Another bottle with 3 mL of OA/ODE (v/v = 1.5:1.5), Gd(CFCOO)$_3$ (0.90 mmol), Yb(CFCOO)$_3$ (0.10 mmol), and CFCOONa (1 mmol) was injected into the solution immediately. The reaction was kept at 310 °C for 1 h in N_2 atmosphere. Then the solution was cooled to room temperature to make the β-$NaGdF_4$:Yb/Er@β-$NaGdF_4$:Yb further crystallization. Then the reaction solution was heated to 310 °C, and another solution contained 3 mL of OA/ODE (v/v = 1.5:1.5), Nd(CFCOO)$_3$ (0.90 mmol), Yb(CFCOO)$_3$ (0.10 mmol), and CFCOONa (1 mmol) was injected immediately. The reaction was kept at 310 °C for 1 h in N_2 atmosphere. The β-$NaGdF_4$:Yb/Er@β-$NaGdF_4$:Yb@β-$NaNdF_4$:Yb nanoparticles were achieved.

Synthesis of UCNPs@MS Nanocomposite Spheres: In a typical procedure, 2 mL of cyclohexane solution (about 5–10 mg mL^{-1}) containing the UCNPs nanoparticles was mixed with 0.1 g of CTAB and 20 mL of water. The mixture was then stirred vigorously to evaporate the cyclohexane solvent at room temperature, resulting in a transparent and clear UCNPs–CTAB water solution. For coating mesoporous silica shells onto UCNPs, 10 mL of the aqueous CTAB-stabilized UCNPs solution was added to the mixture of 20 mL of water, 3 mL of ethanol, and 150 μL of 2 M NaOH solution. The mixture was heated up to 70 °C under stirring. When the temperature was stable, 200 μL of tetraethylorthosilicate (TEOS) was added dropwise and the reaction was allowed to proceed for 10 min. The as-synthesized materials were centrifuged and washed with ethanol three times. The surfactant CTAB was removed via a fast and efficient ion exchange method, where the as-synthesized UCNPs@MS (20 mg) are transferred to 50 mL of ethanol containing 0.3 g of NH_4NO_3 and kept at 60 °C for 2 h. Finally, the as-obtained UCNPs@MS nanocomposite spheres were dispersed in ethanol.

Preparation of Amino-Functionalized UCNPs@MS: First, a ligand exchange approach was adopted to obtain amino-functionalized UCNPs@MS using PAAm. Typically, 50 mL of PAAm (20 wt%) aqueous solution were added to 4 mL of ethanol to form a clear solution after being dispersed with ultrasonic wave. Then 0.2 mL of 20 mmol mL^{-1} solution of UCNPs@MS in ethanol was added. The solution was stirred at room temperature for 36 h. The nanoparticles were obtained after centrifugation and redispersed in water. The PAAm-coated UCNPs@MS provide a terminal amino groups, which can be used for electrostatic attraction of UCNPs@MS with electronegative $Au_{25}(Capt)_{18}^{-}$.

Preparation of Au$_{25}$(Capt)$_{18}^{-}$: Typically, $HAuCl_4{\cdot}3H_2O$ (78.7 mg) and TOAB (0.23 mmol, 126.8 mg) were first dissolved in 10 mL of methanol and vigorously stirred for 20 min. After 20 min, captopril (1 mmol, 217.2 mg) was dissolved in 5 mL of methanol and rapidly injected in the reaction mixture, which was further stirred for 30 min. After 30 min, $NaBH_4$ (2 mmol, 75.6 mg) was dissolved in 5 mL of ice-cold water and rapidly added under vigorous stirring of the reaction mixture. The reaction was further kept for 8 h, and then the reaction mixture was centrifuged to remove insoluble Au(I) polymer. The supernatant was collected and further concentrated by rotary evaporation and then precipitated by adding ethanol. The precipitate was extracted several times with minimum amounts of methanol, and then the extracted clusters were finally precipitated by ethanol and dried in vacuum.

Preparation of Au$_{25}$(Capt)$_{18}^{-}$Loaded UCNPs@MS (UCNPs@MS-Au$_{25}$): Typically, 5 mL of UCNPs@MS solution (5 mg mL^{-1}) was stirred first at room temperature for 2 h. Then 2 mL of $Au_{25}(Capt)_{18}^{-}$ solution (0.8 mg mL^{-1}) was added to above solution, and stirred for 8 h in the dark. The UCNPs@MS-Au_{25} was obtained by centrifugalization and dried in vacuum. The final content of the $Au_{25}(Capt)_{18}^{-}$ in the UCNPs@MS-Au_{25} sample was determined by ICP-MS.

Synthesis of PEG-Modified UCNPs@MS-Au$_{25}$(UCNPs@MS-Au$_{25}$-PEG): Surface modification of poly(ethylene glycol) (PEG) onto UCNPs@MS-Au_{25} was performed according to the method developed previously.

© 2015 WILEY-VCH Verlag GmbH & Co. KGaA, Weinheim

PEG500–silane (30 µL) was added to a mixture of ethanol (30 mL), deionized water (6 mL), NH_4OH (300 µL), and the as-prepared UCNPs@MS-Au_{25} (40 mg). After stirring for 24 h, the UCNPs@MS-Au_{25}-PEG samples were centrifuged several times to remove the unreacted chemicals.

Singlet Oxygen Detection: The $^1O_2$ was detected by a chemical method by using DAB as probe. First, a 10×10^{-3} M stock solution of DAB in *N-N*-dimethylformamide (DMF) was prepared and was then added to 2 mL of an aqueous solution of UCNPs@MS-Au_{25}-PEG to give final concentrations of UCNPs@MS-Au_{25}-PEG and DAB of 40–85 and 500×10^{-6} M, respectively. The solution was immediately purged with air for 10 min in the dark before measurement. The solutions were then irradiated with 808 nm laser (0.5 W cm^{-2}), or 980 nm laser (0.5 W cm^{-2}) for 20 min. These laser power values were measured using a laser power meter (7Z01500, OPHIR, USA). As the control, the Au_{25} sample was also used in the $^1O_2$ detection instead of UCNPs@MS-Au_{25}-PEG, keeping the equal Au content. The adsorption spectra were recorded after different periods of light irradiation.

NIR Laser-Induced In Vitro PTT Effect of UCNPs@MS-Au_{25}-PEG: Briefly, HeLa cells departed into four groups (*n* = 2) were seeded in a 96-well plate with a density of 6000 cells per well and cultured in 5% CO_2 at 37 °C for 24 h. After being rinsed with PBS (pH = 7.4), the cells were incubated with UCNPs@MS-Au_{25}-PEG (group 1 and 2) and Au_{25} (group 3) and without any treatment (group 4) for 4 h at 37 °C under the same conditions. Then the cells were rinsed again with PBS and immersed in 200 µL of fresh culture medium before being illuminated using an 808 nm laser (group 1, 3, and 4) and 980 nm laser (group 2) with same energy density of 2.5 W cm^{-2} for 4 min. During illumination, the temperature and infrared thermographs of the wells in different groups was recorded by the thermal infrared imager (R300SR, NEC).

In Vitro Cell Viability of UCNPs@MS-Au_{25}-PEG: 6000–7000 L929 fibroblast cells were plated in 200 µL media per well in a 96-well plate, then incubated for 24 h at 37 °C with 5% CO_2 to allow the cells to attach to the wells. The UCNPs@MS-Au_{25}-PEG were diluting at concentrations of 0, 50, 100, 200, 400, and 800 µg mL^{-1}, respectively. The solution with different concentration was added to the wells and incubated for another 24 h at 37 °C with 5% CO_2. Then 20 µL (5 mg mL^{-1}) of MTT solution was added to each well containing different amounts of UCNPs@MS-Au_{25}-PEG. The plate was incubated at 37 °C for another 4 h subsequently. During this period, viable cells make MTT reduce into formazan which can be dissolved by DMSO. The absorbance of the suspension was recorded using a microplate reader regulating to 490 nm as detecting wavelength.

In Vitro Cytotoxicity of UCNPs@MS-Au_{25}-PEG Nanoparticles: In vitro cytotoxicity of UCNPs@MS-Au_{25}-PEG nanoparticles was assayed against HeLa cancer cells. HeLa cells departed into four groups (*n* = 5) were seeded in a 96-well plate with a density of 6000 cells per well and cultured in 5% CO_2 at 37 °C for 24 h. HeLa cells in the first three groups were treated with UCNPs@ MS-Au_{25}-PEG for about 4 h, then respectively irradiated with a 808 nm laser for 40 min (2.5 W cm^{-2}, 5 min break after 5 min irradiation, group 1), 980 nm laser for 40 min (2.5 W cm^{-2}, 5 min break after 5 min irradiation, group 2) and without any irradiation (group 3). As the control, the HeLa cells treated with Au_{25} were irradiated with an 808 nm laser for 40 min (2.5 W cm^{-2}, 5 min break after 5 min irradiation, and group 4). Then the cells were incubated for another 48 h in the dark. The concentrations of gold in all groups were 15×10^{-6} M. At the end of the incubation, cells were then treated with 3-[4,5-dimethylthiazol-2-yl]-2,5-diphenyltetrazolium bromide (MTT) solution (diluted in a culture medium with a final concentration of 5 mg mL^{-1}) and incubated for another 4 h. Then the supernatant was removed, and 150 µL of DMSO was added to each well before the plate was examined using a microplate reader at the wavelength of 490 nm. To further identify the cell viability, the cells (in group 1 and 3) were costained by Calcein AM and ethidium homodimer-1 to differentiate live (green) and dead (red) cells, respectively.

Upconversion Luminescence Microscopy (UCLM) Observation of the UCNPs@MS-Au_{25}-PEG Nanoparticles: The instrument of UCLM was rebuilt on an inverted fluorescence microscope (Nikon Ti–S), and an external CW 980 nm diode laser was illuminated onto the samples. HeLa cells (5 × 104 per well) were seeded in 6-well culture plates and grown overnight as a monolayer and were incubated with UCNPs@MS-Au_{25}-PEG at 37 °C for different times. Then, the cells were washed with PBS three times, fixed with 2.5% formaldehyde (1 mL per well) at 37 °C for 10 min, and washed with PBS three times.

Cellular Uptake of the UCNPs@MS-Au_{25}-PEG Nanoparticles: Cellular uptake was examined using CLSM and ICP-MS. For CLSM, the HeLa cells were seeded in 6-well culture plates (a clean coverslip was put in each well) and grown overnight as a monolayer and were incubated with UCNPs@MS-Au_{25}-PEG at 37 °C for different periods, respectively. Thereafter, the cells were rinsed with PBS three times, fixed with 2.5% formaldehyde (1 mL per well) at 37 °C for 10 min, and then rinsed with PBS three times again. The cover slips were placed on a glass microscope slides, and the samples were visualized using CLSM (FV10-ASW). For ICP-MS experiments, HeLa cells (1 × 105) were seeded in 6-well plates. These cells were then treated with UCNPs@MS-Au_{25}-PEG nanoparticles (500 µg), and then incubated at 37 °C for 30 min, 1 h, and 6 h. After being rinsed with PBS three times, the cells were lysed by cell lysis buffer.

Animal Experiments: All animal operations were in accord with institutional animal use and care regulations. Suspension of H22 tumor cells was subcutaneously inoculated into the left armpit of the mice. When the tumors size reached to mean volume of ≈100 mm^3, the mice were random divided into five groups with six mice each group. The UCNPs@MS-Au_{25}-PEG was intravenously injected to the mice of the first two groups in the dark. After 48 h, the tumor site was irradiated with 808 nm laser for 30 min (2.5 W cm^{-2}, 5 min break after 10 min irradiation, group 1) and 980 nm laser for 30 min (2.5 W cm^{-2}, 5 min break after 10 min irradiation, group 2). Group 3 was injected with Au_{25} nanoparticles in the dark and irradiated with the 808 nm laser for 30 min (2.5 W cm^{-2}, 10 min break after 5 min irradiation). The injected Au dose in 80 µL of saline was 0.75 mg kg^{-1} body weight. Similar to group 1, group 4 was exposed to the 808 nm laser for 30 min without injection. Group 5 was only intravenously injected with saline (80 µL) as the control. The mice were anesthetized by chloral hydrate solution (5%, 0.1 mL per mice) and the tumor surface was depilated before irradiation. Tumor diameters were measured every other day with a Vernier caliper in 2D and calculated as volume $V = d^2 \times D/2$ (where *d* is the shortest diameter of tumor, and *D* is the longest diameter of tumor). The body weight of each mouse was also recorded. Relative tumor volume was calculated as V/V_0 (V_0 was the corresponding tumor volume when the treatment was initiated).

Ex Vivo Histological Staining: After 14 d from the phototherapy, the tumors and organs (liver, lung, kidney, heart, and spleen) of the mice in groups were dissected, fixed in a 4% formaldehyde solution for 24 h at room temperature before paraffin embedding. After dehydration, the dry weights of the liver, spleen, and tumor were recorded. After paraffin embedding, fine 5 µm slices of the organs were stained with hematoxylin and eosin and studied for histological changes.

Biodistribution of Nanoparticles in Mice: Female Balb/c mice weighing about 18–20 g were injected with UCNPs@MS-Au_{25}-PEG nanoparticles (26 mg Gd kg^{-1}) intravenously. The mice (*n* = 4) were then euthanized at different time points (10 min, 1 h, 3 h, 12 h, 1 d, 3 d, and 7 d). Major organs (heart, liver, spleen, lung, and kidney) were collected and weighed. Then all the tissues were treated with HNO_3 and H_2O_2 (v/v = 1:2) at 70 °C to obtain clear solutions. The gadolinium and gold concentrations in the solutions were determined by ICP-MS and the contents in each tissue were calculated.

In Vivo Photothermal Imaging of UCNPs@MS-Au_{25}-PEG: Suspension of H22 tumor cells was subcutaneously inoculated into the left armpit of the mice. When the tumor size reached about 100 mm^3, 100 µL of UCNPs@MS-Au_{25}-PEG (400 µg mL^{-1}) was intravenously injected into the tumor-bearing mice. After 48 h, the thermal imaging of different time after injection was recorded by a R300SR-HD infrared camera (NEC) when the tumors were exposed to 808 nm laser (MW-GX-808/5000 mW).

In Vivo Photoacoustic Imaging of UCNPs@MS-Au_{25}-PEG: Suspension of H22 tumor cells was subcutaneously inoculated into the left armpit of the mice. When the tumor size reached about 100 mm^3, 100 μL of UCNPs@MS-Au$_{25}$-PEG (400 μg mL^{-1}) was intravenously injected into the tumor-bearing mice. PA imaging of different time after injection of the tumor site was performed by a Vevo 2100 LAZR system (VisualSonics Inc. New York, NY) equipped with a 40 MHz, 256-element linear array transducer on tumors.

In Vitro and Vivo X-Ray CT Imaging: To perform in vivo CT imaging, the Balb/c mice were first anesthetized with 10% chloral hydrate by intraperitoneal injection. UCNPs@MS-Au$_{25}$-PEG nanoparticles (50 μL, 20 mg mL^{-1}) were intratumorally injected into the tumor-bearing mouse in situ. The mouse was scanned before and after intratumoral injection. For intravenous injection, 200 μL of UCNPs@MS-Au$_{25}$-PEG nanoparticles (50 mg mL^{-1}) was injected into two mice, respectively. CT images were acquired at timed intervals. The in vivo CT imaging was performed on a Philips 256-slice CT scanner (Philips Medical System). Imaging parameters were given as follows: thickness, 0.9 mm; pitch, 0.99; 120 kVp, 300 mA; field of view, 350 mm; gantry rotation time, 0.5 s; and table speed, 158.9 mm s^{-1}. Thin-section axial images were reformed to coronal images by a computational technique referred to as multiplanar reconstruction.

In Vitro T_1-Weighted MR Imaging: The in vitro MR imaging experiments were performed in a 0.5 T MRI magnet (Shanghai Niumai Corporation Ration NM120-Analyst). UCNPs@MS-Au$_{25}$-PEG samples were dispersed in water at various Gd concentrations (by ICP-MS measurement). T_1 was acquired using an inversion recovery sequence. T_1 measurements were performed using a nonlinear fit to changes in the mean signal intensity within each well as a function of repetition time with a Huantong 1.5 T MR scanner. Finally, the r_1 relaxivity values were determined through the curve fitting of $1/T_1$ relaxation time (s^{-1}) versus the Gd concentration (mM).

Characterization: XRD measurements were carried out a Rigaku D/max-TTR-III diffractometer using Cu-Kα radiation (λ = 0.15405 nm). SEM images were measured on a scanning electron microscope (SEM, JSM-6480A, Japan Electronics). TEM and high-resolution transmission electron microscopy (HRTEM) were recorded on a FEI Tecnai G^2 S-Twin with a field emission gun operating at 200 kV. N$_2$ absorption/desorption isotherms were obtained at 77 K using a Micromeritics ASAP TriStar II instrument. The specific surface area was determined through the Brunauer–Emmett–Teller (BET) method. The pore size distribution was calculated by the BJH method. UCL emission spectra were obtained using 980 nm LD Module (K98D08M-30W, China) as the excitation source and detected by R955 (HAMAMATSU) from 400–900 nm. All the UC spectra in the experiment were gained under the same condition with the same signal amplification. UV–vis spectra were detected by UV-1601 spectrophotometer. All the measurements were performed at room temperature.

Supporting Information

Supporting Information is available from the Wiley Online Library or from the author.

Acknowledgements

Financial supports from the National Natural Science Foundation of China (Grant Nos. NSFC 21271053, 21401032, 51472058, and 51332008), Natural Science Foundation of Heilongjiang Province (Grant No. B201403), Harbin Sci.-Tech. Innovation Foundation (Grant No. 2014RFQXJ019), and Fundamental Research Funds for the Central Universities of China (Grant No. HEUCF1412) are greatly acknowledged.

Received: February 4, 2015
Revised: March 31, 2015
Published online: May 22, 2015

[1] Q. Ju, D. Tu, Y. Liu, R. Li, H. Zhu, J. Chen, Z. Chen, M. Huang, X. Chen, *J. Am. Chem. Soc.* **2012**, *134*, 1323.
[2] a) P. P. Yang, S. L. Gai, J. Lin, *Chem. Soc. Rev.* **2012**, *41*, 3679; b) N. M. Idris, M. K. Gnanasammandhan, J. Zhang, P. C. Ho, R. Mahendran, Y. Zhang, *Nat. Med.* **2012**, *18*, 1580.
[3] X. M. Li, F. Zhang, D. Y. Zhao, *Nano Today* **2013**, *8*, 643.
[4] Q. Liu, Y. Sun, C. G. Li, J. Zhou, C. Y. Li, T. S. Yang, X. Z. Zhang, T. Yi, D. M. Wu, F. Y. Li, *ACS Nano* **2011**, *5*, 3146.
[5] M. Haase, H. Schaefer, *Angew. Chem. Int. Ed.* **2011**, *50*, 5808.
[6] C. Wang, L. Cheng, Y. M. Liu, X. J. Wang, X. X. Ma, Z. Y. Deng, Y. G. Li, Z. Liu, *Adv. Funct. Mater.* **2013**, *23*, 3077.
[7] J. Q. Hu, Q. Li, J. H. Zhan, Y. Jiao, Z. W. Liu, S. P. Ringer, Y. Bando, D. Golberg, *ACS Nano* **2008**, *2*, 107.
[8] Q. Chen, C. Wang, L. Cheng, W. W. He, Z. Cheng, Z. Liu, *Biomaterials* **2014**, *35*, 2915.
[9] C. Wang, H. Q. Tao, L. Cheng, Z. Liu, *Biomaterials* **2011**, *32*, 6145.
[10] J. Zhou, Z. Liu, F. Y. Li, *Chem. Soc. Rev.* **2012**, *41*, 1323.
[11] F. Chen, W. Bu, W. Cai, J. Shi, *Curr. Mol. Med.* **2013**, *13*, 1613.
[12] X. J. Xie, N. Y. Gao, R. R. Deng, Q. Sun, Q. H. Xu, X. G. Liu, *J. Am. Chem. Soc.* **2013**, *135*, 12608.
[13] Q. W. Tian, M. H. Tang, Y. G. Sun, R. J. Zou, Z. G. Chen, M. F. Zhu, S. P. Yang, J. L. Wang, J. H. Wang, J. Q. Hu, *Adv. Mater.* **2011**, *23*, 3542.
[14] Y. H. Wang, H. G. Wang, D. P. Liu, S. Y. Song, X. Wang, H. J. Zhang, *Biomaterials* **2013**, *34*, 7715.
[15] Z. X. Zhao, Y. N. Han, C. H. Lin, D. Hu, F. Wang, X. L. Chen, Z. Chen, N. F. Zheng, *Chem. Asian J.* **2012**, *7*, 830.
[16] R. Vankayala, C. C. Lin, P. Kalluru, C. S. Chiang, K. C. Hwang, *Biomaterials* **2014**, *35*, 5527.
[17] X. Xia, X. G. Kong, X. M. Liu, L. P. Tu, Y. L. Zhang, Y. L. Chang, K. Liu, D. Z. Shen, H. Y. Zhao, H. Zhang, *Biomaterials* **2014**, *35*, 4146.
[18] X. Yin, Y. W. Zhang, L. D. Sun, C. H. Yan, *Nanoscale* **2010**, *2*, 953.
[19] Z. J. Gu, L. Yan, G. Tian, S. J. Li, Z. F. Chai, Y. L. Zhao, *Adv. Mater.* **2013**, *25*, 3758.
[20] L. Cheng, K. Yang, Y. G. Li, X. Zeng, M. W. Shao, S. T. Lee, Z. Liu, *Biomaterials* **2012**, *33*, 2215.
[21] X. C. Ye, J. E. Collins, Y. J. Kang, J. Chen, D. T. N. Chen, A. G. Yodh, C. B. Murray, *Proc. Natl. Acad. Sci. U.S.A.* **2010**, *107*, 22430.
[22] G. F. Wang, Q. Peng, Y. D. Li, *Acc. Chem. Res.* **2011**, *44*, 322.
[23] L. Y. Wang, Y. D. Li, *Chem. Mater.* **2007**, *19*, 727.
[24] Y. T. Zhong, G. Tian, Z. J. Gu, Y. J. Yang, L. Gu, Y. L. Zhao, Y. Ma, J. N. Yao, *Adv. Mater.* **2014**, *26*, 2831.
[25] H. Wen, H. Zhu, X. Chen, T. F. Hung, B. Wang, G. Zhu, S. F. Yu, F. Wang, *Angew. Chem. Int. Ed.* **2013**, *52*, 13419.
[26] Y. F. Wang, G. Y. Liu, L. D. Sun, J. W. Xiao, J. C. Zhou, C. H. Yan, *ACS Nano* **2013**, *7*, 7200.
[27] U. Rocha, K. U. Kumar, C. Jacinto, I. Villa, F. Sanz-Rodriguez, M. D. I. de la Cruz, A. Juarranz, E. Carrasco, F. van Veggel, E. Bovero, J. G. Sole, D. Jaque, *Small* **2014**, *10*, 1141.
[28] B. Tian, C. Wang, S. Zhang, L. Z. Feng, Z. Liu, *ACS Nano* **2011**, *5*, 7000.
[29] P. Huang, J. Lin, W. Li, P. Rong, Z. Wang, S. Wang, X. Wang, X. Sun, M. Aronova, G. Niu, R. D. Leapman, Z. Nie, X. Chen, *Angew. Chem. Int. Ed.* **2013**, *52*, 13958.
[30] G. Terentyuk, E. Panfilova, V. Khanadeev, D. Chumakov, E. Genina, A. Bashkatov, V. Tuchin, A. Bucharskaya, G. Maslyakova, N. Khlebtsov, B. Khlebtsov, *Nano Res.* **2014**, *7*, 325.
[31] W. S. Kuo, Y. T. Chang, K. C. Cho, K. C. Chiu, C. H. Lien, C. S. Yeh, S. J. Chen, *Biomaterials* **2012**, *33*, 3270.
[32] W. Zheng, S. Zhou, Z. Chen, P. Hu, Y. Liu, D. Tu, H. Zhu, R. Li, M. Huang, X. Chen, *Angew. Chem. Int. Ed.* **2013**, *52*, 6671.
[33] B. Jang, J. Y. Park, C. H. Tung, I. H. Kim, Y. Choi, *ACS Nano* **2011**, *5*, 1086.

© 2015 WILEY-VCH Verlag GmbH & Co. KGaA, Weinheim

[34] T. Murakami, H. Nakatsuji, M. Inada, Y. Matoba, T. Umeyama, M. Tsujimoto, S. Isoda, M. Hashida, H. Imahori, *J. Am. Chem. Soc.* **2012**, *134*, 17862.
[35] J. Shen, L. Zhao, G. Han, *Adv. Drug Delivery Rev.* **2013**, *65*, 744.
[36] M. Guo, H. J. Mao, Y. L. Li, A. J. Zhu, H. He, H. Yang, Y. Y. Wang, X. Tian, C. C. Ge, Q. L. Peng, X. Y. Wang, X. L. Yang, X. Y. Chen, G. Liu, H. B. Chen, *Biomaterials* **2014**, *35*, 4656.
[37] H. H. Gorris, O. S. Wolfbeis, *Angew. Chem. Int. Ed.* **2013**, *52*, 3584.
[38] C. J. Carling, F. Nourmohammadian, J. C. Boyer, N. R. Branda, *Angew. Chem. Int. Ed.* **2010**, *49*, 3782.
[39] N. Lee, S. H. Choi, T. Hyeon, *Adv. Mater.* **2013**, *25*, 2641.
[40] D. L. Ni, J. W. Zhang, W. B. Bu, H. Y. Xing, F. Han, Q. F. Xiao, Z. W. Yao, F. Chen, Q. J. He, J. N. Liu, S. J. Zhang, W. P. Fan, L. P. Zhou, W. J. Peng, J. L. Shi, *ACS Nano* **2014**, *8*, 1231.
[41] N. Lee, H. R. Cho, M. H. Oh, S. H. Lee, K. Kim, B. H. Kim, K. Shin, T. Y. Ahn, J. W. Choi, Y. W. Kim, S. H. Choi, T. Hyeon, *J. Am. Chem. Soc.* **2012**, *134*, 10309.
[42] Q. F. Xiao, X. P. Zheng, W. B. Bu, W. Q. Ge, S. J. Zhang, F. Chen, H. Y. Xing, Q. G. Ren, W. P. Fan, K. L. Zhao, Y. Q. Hua, J. L. Shi, *J. Am. Chem. Soc.* **2013**, *135*, 13041.
[43] S. J. Zeng, H. B. Wang, W. Lu, Z. G. Yi, L. Rao, H. R. Liu, J. H. Hao, *Biomaterials* **2014**, *35*, 2934.
[44] E. N. M. Cheung, R. D. A. Alvares, W. Oakden, R. Chaudhary, M. L. Hill, J. Pichaandi, G. C. H. Mo, C. Yip, P. M. Macdonald, G. J. Stanisz, F. van Veggel, R. S. Prosser, *Chem. Mater.* **2010**, *22*, 4728.
[45] J. H. Hao, Y. Zhang, X. H. Wei, *Angew. Chem. Int. Ed.* **2011**, *50*, 6876.
[46] D. J. Gargas, E. M. Chan, A. D. Ostrowski, S. Aloni, M. V. P. Altoe, E. S. Barnard, B. Sanii, J. J. Urban, D. J. Milliron, B. E. Cohen, P. J. Schuck, *Nat. Nanotechnol.* **2014**, *9*, 300.
[47] H. Q. Wang, T. Nann, *ACS Nano* **2009**, *3*, 3804.
[48] J. C. Boyer, L. A. Cuccia, J. A. Capobianco, *Nano Lett.* **2007**, *7*, 847.
[49] R. Martin-Rodriguez, S. Fischer, I. Aruna, B. Froehlich, K. W. Kramer, J. C. Goldschmidt, B. S. Richards, A. Meijerink, *Chem. Mater.* **2013**, *25*, 1912.
[50] J. Lin, S. J. Wang, P. Huang, Z. Wang, S. H. Chen, G. Niu, W. W. Li, J. He, D. X. Cui, G. M. Lu, X. Y. Chen, Z. H. Nie, *ACS Nano* **2013**, *7*, 5320.
[51] Z. Liu, S. Tabakman, K. Welsher, H. J. Dai, *Nano Res.* **2009**, *2*, 85.
[52] H. F. Zhang, K. Maslov, G. Stoica, L. H. V. Wang, *Nat. Biotechnol.* **2006**, *24*, 848.
[53] M. Gobin, M. H. Lee, N. J. Halas, W. D. James, R. A. Drezek, J. L. West, *Nano Lett.* **2007**, *7*, 1929.
[54] X. H. Huang, I. H. El-Sayed, W. Qian, M. A. El-Sayed, *J. Am. Chem. Soc.* **2006**, *128*, 2115.
[55] C. Loo, A. Lin, L. Hirsch, M. H. Lee, J. Barton, N. J. Halas, J. West, R. Drezek, *Technol. Cancer Res. Treat.* **2004**, *3*, 33.
[56] G. S. Song, Q. A. Wang, Y. Wang, G. Lv, C. Li, R. J. Zou, Z. G. Chen, Z. Y. Qin, K. K. Huo, R. G. Hu, J. Q. Hu, *Adv. Funct. Mater.* **2013**, *23*, 4281.
[57] Y. M. Yang, Q. Shao, R. R. Deng, C. Wang, X. Teng, K. Cheng, Z. Cheng, L. Huang, Z. Liu, X. G. Liu, B. G. Xing, *Angew. Chem. Int. Ed.* **2012**, *51*, 3125.
[58] Y. Zhu, H. F. Qian, B. A. Drake, R. C. Jin, *Angew. Chem. Int. Ed.* **2010**, *49*, 1295.
[59] H. Kawasaki, S. Kumar, G. Li, C. J. Zeng, D. R. Kauffman, J. Yoshimoto, Y. Iwasaki, R. C. Jin, *Chem. Mater.* **2014**, *26*, 2777.
[60] D. Evanko, *Nat. Methods* **2011**, *8*, 448.
[61] M. J. Steinbeck, A. U. Khan, W. H. Appel Jr., M. J. Karnovsky, *J. Histochem. Cytochem.* **1993**, *41*, 1659.
[62] H. Kawasaki, S. Kumar, G. Li, C. J. Zeng, D. R. Kauffman, J. Yoshimoto, Y. Iwasaki, R. C. Jin, *Chem. Mater.* **2014**, *26*, 2777.
[63] S. Kumar, R. C. Jin, *Nanoscale* **2012**, *4*, 4222.
[64] C. Zhang, Z. Zhou, Q. Qian, G. Gao, C. Li, L. Feng, Q. Wang, D. Cui, *J. Mater. Chem. B* **2013**, *1*, 5045.

© 2015 WILEY-VCH Verlag GmbH & Co. KGaA, Weinheim